ACS OMEGA

http://pubs.acs.org/journal/acsodf

Article

Assembling Au_4 Tetrahedra to 2D and 3D Superatomic Crystals Based on Superatomic-Network Model

Chen Yan, Jiuqi Yi, Peng Wang, Dan Li,* and Longjiu Cheng*

Cite This: *ACS Omega* 2022, 7, 32708−32716

Read Online

ACCESS | Metrics & More | Article Recommendations | Supporting Information

ABSTRACT: Thiolate-protected gold nanoclusters (denoted as $Au_m(SR)_n$ or Au_nL_m) have received extensive attention both experimentally and theoretically. Understanding the growth mode of the Au_4 unit in $Au_m(SR)_n$ is of great significance for experimental synthesis and the search for new gold clusters. In this work, we first build six clusters of $Au_7(AuCl_2)_3$, $Au_{12}(AuCl_2)_4$, $Au_{16}(AuCl_2)_6$, $Au_{22}(AuCl_2)_6$, and $Au_{30}(AuCl_2)_6$ with the Au_4 unit as the basic building blocks. Density functional theory (DFT) calculations show that these newly designed clusters have high structural and electronic stabilities. Based on chemical bonding analysis, the electronic structures of these clusters follow the superatom network (SAN) model. Inspired by the cluster structures, we further predicted an Au_4 two-dimensional (2D) monolayer and a three-dimensional (3D) crystal using graphene and diamond as templates, respectively. The computational results demonstrate that the two structures have high dynamic, thermal, and mechanical stabilities, and both structures exhibit metallic properties according to the band structures calculated at the HSE06 level. The chemical bonding analysis by the solid-state natural density partitioning (SSAdNDP) method indicates that they are superatomic crystals assembled by two electron Au_4^- superatoms. With this construction strategy, the new bonding pattern and properties of Au_nL_m are studied and the structure types of gold are enriched.

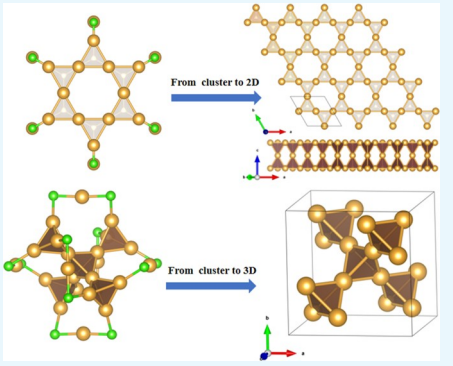

1. INTRODUCTION

Thiolate-protected gold nanoclusters (donated as $Au_m(SR)_n$ or Au_nL_m) have become a research hotspot in the field of nanoscience owing to their unique physicochemical properties.[1−7] Since the structure determination of $Au_{102}(SR)_{44}$[8] and $Au_{25}(SR)_{18}^-$,[9,10] a large amount of $Au_m(SR)_n$ has been successfully characterized.[11−17] Particularly, due to the relatively outstanding chemical stability of $Au_m(SR)_n$, enormous efforts have been devoted to the study of $Au_m(SR)_n$ both experimentally and theoretically.[18−21] On this basis, the structure evolution behaviors of $Au_n(SR)_m$ were further explored.[22,23] According to X-ray single-crystal diffraction analyses of $Au_m(SR)_n$, some gold atoms were arranged in an ordered Au core. The rest of the gold atoms were combined with the ligands to form a series of gold−thiolate protecting units (e.g., −RS−Au−SR− and −RS−Au−SR−Au−SR−, also called staple motifs) capping the Au core. As more $Au_m(SR)_n$ structures were acquired, it was found that these clusters possessed diverse configurations of core structures. In addition, the types and the numbers of staple motifs were extremely sensitive to the number of gold atoms and thiolate ligands.

The structure determination of thiolate-protected gold nanoclusters provides an effective theoretical model for understanding the relationship between their structures and properties. The "divide and protect" model was first proposed by Häkkinen et al..[24] In this model, $Au_m(SR)_n$ can be viewed as an Au core protected by different staple motifs.[25−30] Pei et al. developed a structural partition formula for $Au_m(SR)_n$ (presented as $Au_{a+a'}[Au(SR)_2]_b[Au_2(SR)_3]_c[Au_3(SR)_4]_d$..., where a, a', b, c, d, ... were integers[31]), which was first applied to the experimentally synthesized $Au_{38}(SR)_{24}$.[32] Following the proposed structural partition formula, a low-energy isomer of $Au_{38}(SR)_{24}$ was acquired and written as $[Au]_{5+18}[Au(SR)_2]_3[Au_2(SR)_3]_6$, which was in good agreement with later experimental reports.[33] Some $Au_m(SR)_n$ clusters with magic numbers were well explained by the superatom complex (SAC) concept based on the jellium model,[34] such as $Au_{15}(SR)_{13}$,[35] $Au_{25}(SR)_{18}^-$,[9] and $Au_{44}(SR)_{26}$,[36] having 2, 8, and 18 free valence electrons, respectively.

However, not all of the gold nanoclusters satisfy the framework of the SAC model. Cheng et al. developed the super valance bond (SVB) model[37−39] to explain the electronic stability of nonspherical shells of $Au_{38}(SR)_{24}$ metal clusters.[40] Nonetheless, the high stability of some low-symmetry ligand-protected gold nanoclusters also cannot be clearly explained. Subsequently, the superatom network (SAN) model[41] was proposed by Cheng et al., combined with the adaptive natural density partitioning (AdNDP) method, to explain the

Received: July 12, 2022
Revised: July 28, 2022
Accepted: August 3, 2022
Published: August 30, 2022

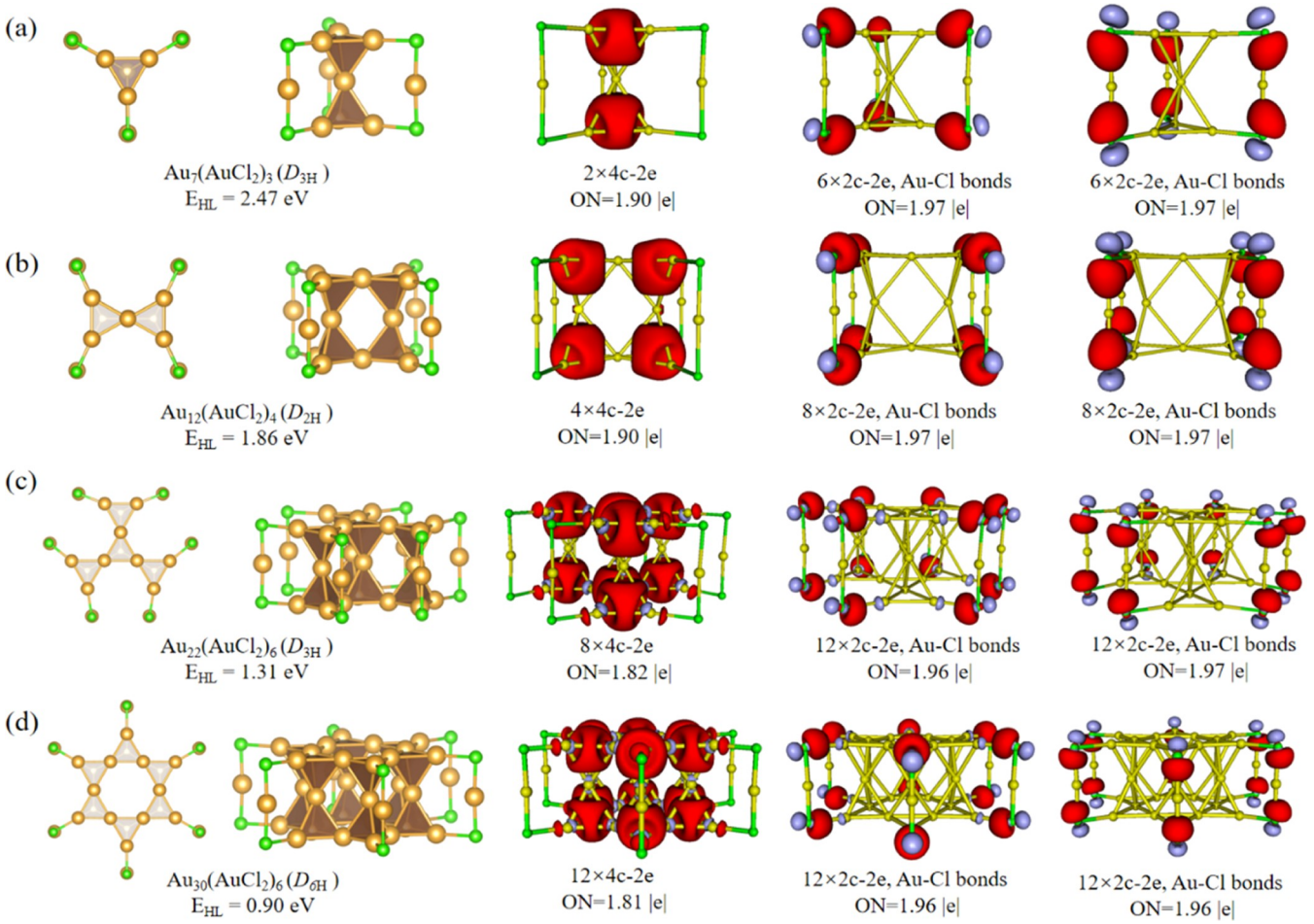

Figure 1. Optimized geometric structure and AdNDP localized natural bonding orbitals of (a) $Au_7(AuCl_2)_3$, (b) $Au_{12}(AuCl_2)_4$, (c) $Au_{22}(AuCl_2)_6$, and (d) $Au_{30}(AuCl_2)_6$ clusters. Au, yellow and Cl, green.

electronic stability. The Au core of these gold clusters can be viewed as networks of nonconjugated 4-center-2-electron (4c-2e) tetrahedral Au_4 superatoms.[42] The experimentally synthesized $Au_{18}(SR)_{14}$,[43] $Au_{20}(SR)_{16}$,[44] $Au_{22}(SR)_{18}$,[45] and $Au_{24}(SR)_{20}$[46] are compounds with four valance electrons, following the SAN model. $Au_{18}(SR)_{14}$ is composed of an Au_9 core and five staple motifs. According to the SAN model, the Au_9 core can be regarded as a unique combination of two fused superatom octahedral Au_6 units. The structure of $Au_{20}(SR)_{16}$ features a vertex-sharing bi-tetrahedral Au_7 kernel and a "ring" motif $Au_8(SR)_8$. The structure of $Au_{22}(SR)_{18}$ also has an Au_7 kernel, which is surrounded by one $Au_6(SR)_6$ and three $Au_3(SR)_4$ motifs. This Au_7 kernel is formed by two Au_4 units sharing vertices. The structure of $Au_{24}(SR)_{20}$ has a bi-tetrahedral Au_8 kernel protected by two pairs of tetrameric staples. According to the SAN model, the Au kernels of these three clusters can all be seen as networks of two Au_4 superatoms. In addition, Pei et al. reported many $Au_m(SR)_n$ clusters with face-centered-cubic (fcc) type of Au_4 kernel.[47,48] These clusters have a unique growth pattern and grow into a double-helix structure through the Au_4 unit sharing the vertex, such as $Au_{36}(SR)_{24}$,[49] $Au_{44}(SR)_{28}$,[17] $Au_{52}(SR)_{32}$,[50] $Au_{60}(SR)_{36}$,[51] and $Au_{76}(SR)_{44}$[52] clusters. The thiolate-protected gold nanowire (RS-AuNW) can be obtained by infinite growth according to its growth mode. Moreover, the $Au_{44}(SR)_{28}$ cluster was confirmed by Jin et al.[53] Therefore, the developed theoretical models not only logicalize the existing structures but also facilitate the design of new structures.

Because the synthesis and characterization of thiolate-protected gold nanoclusters remain challenging, density functional theory (DFT) calculations play a prominent part in structural prediction.[54,55] The tetrahedral Au_4 unit is a basic block in thiolate-protected gold nanoclusters and is often used to predict new $Au_m(SR)_n$ clusters and crystal materials.[56−59] In this work, we predicted five $Au_m(SR)_n$ clusters based on the SAN model, using the tetrahedral Au_4 unit as basic building blocks, including $Au_{10}(SR)_6$, $Au_{16}(SR)_8$, $Au_{28}(SR)_{12}$, $Au_{36}(SR)_{12}$, and $Au_{22}(SR)_{12}$. DFT calculations show that these clusters have high electronic and structural stabilities. Based on the growth patterns of these clusters, a graphene-like two-dimensional (2D) Au_4 monolayer and a diamond-like three-dimensional (3D) Au_4 solid were predicted to be stable. Both the 2D-Au_4 monolayer and 3D Au_4 solid have strong light absorption ability. This cluster assembly material based on cluster superatoms can be regarded as an extension of the SAN complexes.

2. COMPUTATIONAL METHOD AND DETAILS

Geometry optimizations, frequency analyses, and electronic properties calculations of all cluster structures were carried out at the PBE[60] level of theory with the def2tzvp basis set[61] as implemented in the Gaussian 09 package.[62] Considering the computational cost, we used halogen (Cl) instead of thiolate

https://doi.org/10.1021/acsomega.2c04391
ACS Omega 2022, 7, 32708−32716

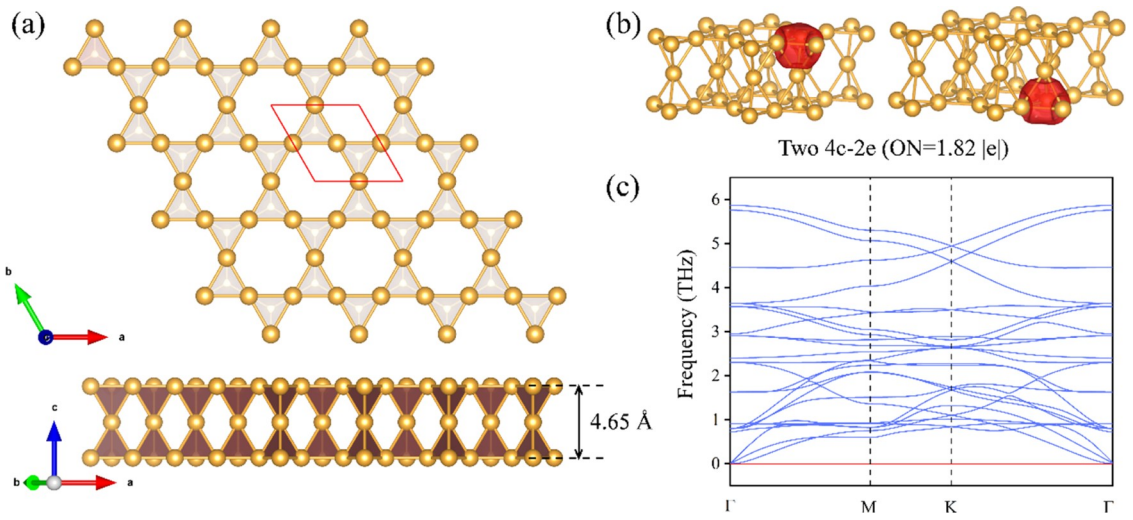

Figure 2. (a) Top and side views of the Au_4 monolayer. The primitive cell is outlined by red lines in this work. (b) Schematic of the SSAdNDP chemical bonding pattern of the Au_4 monolayer. (c) Phonon spectrum of the Au_4 monolayer along the high-symmetry points in the Brillouin zone.

(SR) to complete the calculation because Cl and SR are isolobal ligands.[63] All clusters were verified by frequency check to be true local minimum on the potential energy surface. DFT calculations of the Au_4 monolayer and the Au_4 bulk structure were performed in the Vienna ab initio simulation page (VASP) code.[64] The ion−electron interaction was described by the projector-augmented plane-wave (PAW) method.[65] Generalized gradient approximation (GGA)[60] was used for treating the exchange-correlation functional within the Perdew−Burke−Ernzerhof (PBE)[66] functional form. During the geometry optimizations, the energy cutoff of the plane wave was set to 450 eV. The Brillouin zone was represented by $5 \times 5 \times 1$ and $6 \times 6 \times 6$ Monkhorst−Pack k-point mesh for the Au_4 monolayer and Au_4 solid, respectively. The Hellmann−Feynman force convergence criterion was less than 0.01 eV $Å^{-1}$ and the self-consistent field procedures were performed with an energy of 10^{-6} eV for the total energy. To eliminate the effect between adjacent Au_4 layers, a vacuum distance of ∼15 Å was used. For multilayers, the intralayer van der Waals interactions were corrected by the DFT-D3 approach in Grimme's scheme.[67]

To research the dynamic stability of the materials, we utilized the PHONOPY code[68] to calculate the phonon dispersion spectra. To assess the thermal stability of the periodical structure, ab initio molecular dynamic (AIMD) was carried out by the Nosé−Hoover method.[69] The AIMD simulation in an NVT canonical ensemble (constant number, volume, and temperature) with a time step of 1.0 fs lasts for 5 ps at 300 K. In addition, the Heyd−Scuseria−Ernzerhof (HSE06) hybrid functional[70] was used to reach more accurate electronic band structures. The chemical bonding analyses were calculated by adopting the (solid state) adaptive natural density partitioning ((SS)AdNDP) method,[71−74] which can demonstrate the chemical bonding pattern of delocalized bonds.[75,76] We chose the def2tzvp basis set for the plane-wave projection of the electron density matrix in the solid-state natural density partitioning SSAdNDP calculation.

3. RESULTS AND DISCUSSION

3.1. Geometric and Electronic Characters of $Au_7(AuCl_2)_3$, $Au_{12}(AuCl_2)_4$, $Au_{22}(AuCl_2)_6$, and $Au_{30}(AuCl_2)_6$ Clusters. It is well known that a series of $Au_n(SR)_m$ clusters have been successfully synthesized and designed with the bi-tetrahedral Au_7 unit as a building block, such as $Au_{20}(SR)_{16}$,[77] $Au_{22}(SR)_{18}$,[47] and $Au_{24}(SR)_{20}$.[78] Here, according to the SAN model, we build an $Au_7(AuCl_2)_3$ cluster, which features a vertex-sharing bi-tetrahedral Au_7 core protected by three [Cl−Au−Cl] ligands. The optimized $Au_7(AuCl_2)_3$ cluster with a fairly large highest occupied molecular orbital−lowest unoccupied molecular orbital (HOMO−LUMO) gap (E_{HL}) of 2.47 eV is shown in Figure 1a, indicating high electronic stability. The average Au−Au bond length within the Au_4 tetrahedrons is 2.70−2.77 Å. The bond lengths of Au−Cl are 2.39 Å. Au ($5d^{10}6s^1$) has one free valence electron, and each Au atom of the three Au atoms in the Au_4 unit transfers 0.5 valence electrons to the surrounding Cl atoms to satisfy the 8 electron rule. The remaining centered Au atom contributes 0.5 valence electrons to each Au_4 unit. Thus, the whole Au_4 unit has two valence electrons in total, donated as the Au_4 (2e) superatom. To clearly understand the bonding mode of the monomer, chemical bonding analyses were carried out by the AdNDP method. The results show that $Au_7(AuCl_2)$ has two 4c-2e Au_4 σ bonds with the occupancy numbers (ON) = 1.90 |e| and twelve 2c-2e Au−Cl σ bonds with ON = 1.97 |e|.

Next, we adopt $Au_7(AuCl_2)$ as a monomer to design a dimer. The dimer is composed of four [Cl−Au−Cl] ligands and an Au_{12} core, which is formed by two bi-tetrahedral Au_7 units via sharing two Au atoms. Figure 1b shows that the optimized dimer $Au_{12}(AuCl_2)_4$ has an E_{HL} of 1.86 eV, and the dimer contains four 4c-2e Au_4 σ bonds with ON = 1.90 |e|. The bond lengths of Au−Cl are 2.39 Å, and the Au−Au bond lengths within the Au_4 tetrahedra are in the range of 2.70−2.80 Å. Following a similar construction method, tetramer $Au_{22}(AuCl_2)_6$ and hexamer $Au_{30}(AuCl_2)_6$ are designed and shown in Figure 1c,d, respectively. Their Au−Au bond lengths within the Au_4 tetrahedra are in the range of 2.70−2.83 Å, and the Au−Cl bond lengths are 2.41 Å. The AdNDP results indicate that $Au_{22}(AuCl_2)_6$ and $Au_{30}(AuCl_2)_6$ clusters have eight 4c-2e σ bonds with ON = 1.82 |e| and twelve 4c-2e σ bonds with ON = 1.81 |e|, respectively.

The nucleus-independent chemical shift (NICS) method[79] is widely used to measure the aromaticity of delocalized bonds. It has been successfully used to confirm many Au_4 superatomic

https://doi.org/10.1021/acsomega.2c04391
ACS Omega 2022, 7, 32708−32716

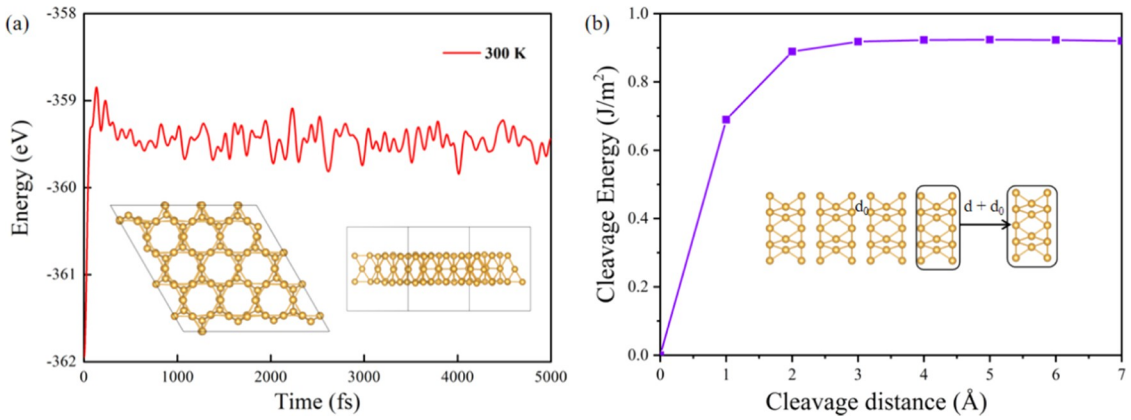

Figure 3. (a) Energy fluctuation depending on the simulated time at 300 K and the snapshot of the Au_4 monolayer after a 5 ps AIMD simulation. (b) Schematic of the cleavage process of the Au_4 monolayer.

systems.[41,42] Here, we perform a NICS method to further prove the existence of Au_4 superatoms. We take the $Au_7(AuCl_2)_3$ cluster as a test. The NICS scan points are located at the geometric center of Au_4 units, and the corresponding NICS values are both −26.8 ppm, which is much more negative than that of benzene (−9.7 ppm).[80] This strong aromaticity indicates electron delocalization with shell closure in the Au_4 core, which confirms the presence of Au_4 superatoms.

3.2. Geometric Structure, Stability, and Electronic Character of the Au_4 Monolayer. The cyclic hexamer $Au_{30}(AuCl_2)_6$ has a similar structure to benzene and can be extended to a graphene-like Au_4 monolayer. As shown in Figure 2a, the space group of the monolayer is *P6/mmm* (number 191, $a = b = 5.45$ Å, and $c = 15$ Å), where one unit cell is composed of eight Au atoms. Similar to the clusters, adjacent Au_4 units are connected by a shared Au atom. The structure of the Au_4 monolayer is a three-layered sandwich structure, similar to the recently discovered AlB_6 monolayer with high stability, unique motif, and superconductivity.[81] The average length of the Au−Au bond in this monolayer is 2.77 Å. For the Au_4 monolayer, we use the SSAdNDP method to analyze its bond patterns. According to the results, there are five d-type localized lone pairs (LPs) on each Au atom with ON = 1.91−2.00 |e| as shown in Figure S1. Therefore, it is implied that they are not involved in the bonding process. Figure 2b shows the 4c-2e Au_4 σ bonds (ON = 1.82 |e|) in each Au_4 unit. Similar to the previously predicted Cu_2Si and Cu_2Ge monolayers, their special 4c-2e bonds lead to strong connections between atoms, thereby enhancing the stability of the structure.[82,83]

Although the Au_4 monolayer has rather intriguing structural properties, the stability of the structure is still unknown. To assess the relative stability of this material, we first calculate the cohesive energy $E_{coh,Au4\text{-}monolayer} = (mE_{Au\text{-}atom} - E_{Au4\text{-}monolayer})/m$, where m, $E_{Au\text{-}atom}$, and $E_{Au4\text{-}monolayer}$ are the atom number, the total energies of a single Au atom, and one unit cell of the Au_4 monolayer, respectively. The cohesive energy of the Au_4 monolayer is 2.63 eV per atom, indicating that the Au_4 monolayer has a strongly bonded network. To verify the kinetic stability of the Au_4 monolayer, we perform phonon dispersion calculations for its geometric configuration (Figure 2c). All positive frequencies in the first Brillouin zone indicate kinetic stability. Moreover, we perform AIMD simulations with a supercell (containing 4 × 4 × 1 primitive cell involving 144 Au atoms) to examine its thermal stability, where the time step and time duration are 1.0 fs and 5 ps, respectively. As shown in Figure 3a, the Au_4 monolayer can maintain its structural integrity at 300 K in AIMD simulations, indicating its thermal stability. Moreover, it can be seen from Figure S2 that the structure of the Au_4 monolayer can maintain its integrity, whereas the structure breaks at 1000 K. Therefore, the melting point of the Au_4 monolayer is between 700 and 1000 K. We also study the mechanical properties of the Au_4 monolayer by calculating the elastic constants, Young's modulus (E), and Poisson's ratio (ν), and the results are listed in Table 1. For this monolayer, the elastic constants satisfy $C_{11}C_{22} - C_{12}^2 > 0$ and $C_{66} > 0$, suggesting its mechanical stability.[84]

Table 1. Calculated Elastic Constants (C_{ij}, in N m^{-1}), Young's Modulus (E, in N m^{-1}), and Poisson's Ratio (ν) for the Au_4 Monolayer

structure	C_{11}	C_{12}	C_{66}	E	ν
2D-Au_4	71.06	29.34	20.86	58.95	0.41

Generally speaking, mechanical and liquid striping techniques are widely used to prepare most 2D materials.[85,86] Here, the process of mechanical striping is studied theoretically. The cleavage energy (E_{cl}) is the minimum energy required during the exfoliation process. We first constructed a five-layer slab, four layers of which were fixed with the monolayer being removable. As shown in the schematic of Figure 3b, d is the separation distance between the exfoliated top layer and the remanent four layers, and d_0 (2.70 Å) is the original interlayer distance of bulk. The cleavage energy is defined as $E_{cl} = E_d - E_{Au4\text{-}monolayer}$, where E_d and $E_{Au4\text{-}monolayer}$ are the separation distance d and no separation energy between the exfoliated top layer and the remanent four layers, respectively.[87,88] It can be seen that as the separation distance increases, the cleavage energy gradually increases, and finally converges to a constant value of 0.91 J m^{-2}, which has the same order of magnitude as the experimentally measured value of graphene (0.37 J m^{-2}).[89] Therefore, the results indicate that it is possible to exfoliate Au_4 monolayer by the mechanical method from its bulk structure experimentally.

We further investigated the electronic properties of the Au_4 monolayer by calculating the band structures and projected density of states (PDOS) at the HSE06 level. As shown in Figure 4a, there is a valence band (VB) passing through the

https://doi.org/10.1021/acsomega.2c04391
ACS Omega 2022, 7, 32708−32716

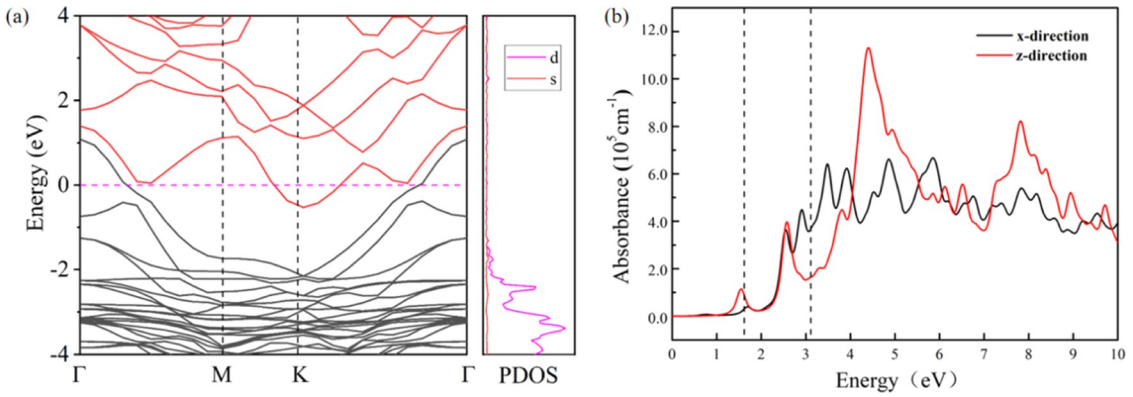

Figure 4. (a) Electronic band structure and projected density of states (PDOS) of the Au_4 monolayer at the HSE06 level. Fermi levels are set to zero and marked with pink dashed lines. (b) Optical absorption coefficient along the *x*- and *z*-directions of the Au_4 monolayer.

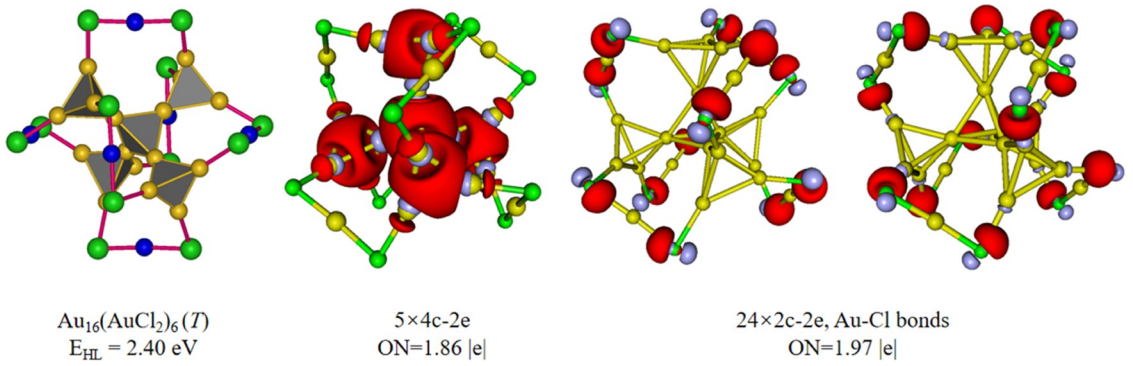

Figure 5. Optimized geometric structure and AdNDP localized natural bonding orbitals of the $Au_{16}(AuCl_2)_6$ cluster. Au, yellow and Cl, green.

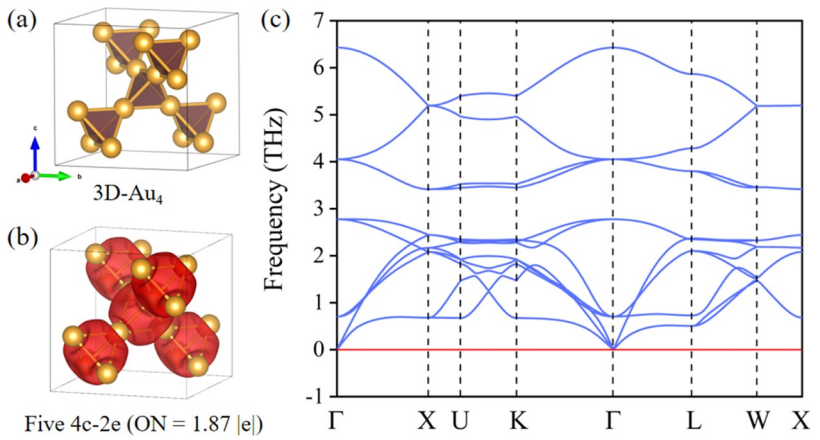

Figure 6. (a) Unit cell structure of the Au_4 crystal. (b) Bond and occupation number of Au_4 unit cell obtained from SSAdNDP analyses. (c) Phonon spectrum for the Au_4 crystal.

Fermi level, and the monolayer exhibits metallic properties. It is also worth noting that the valence band maximum (VBM) is slightly separated from the conduction band minimum (CBM), so there is a tendency to open the band gap. The projected density of states (PDOS) show that the valence band (VB) energy states are mainly contributed by the d orbitals of Au atoms.

The unique optical properties of gold nanomaterials make it of great application value in surface plasmon optics, information storage, surface-enhanced Raman scattering (SERS), and sensing devices. We further calculated the optical absorption spectrum of the Au_4 monolayer by the HSE06 method as shown in Figure 4b. The area within the dotted line is in the visible-light range. The Au_4 monolayer has no anisotropy in *x*- and *y*-directions, so we analyze the optical properties in the *x*- and *z*-directions. The Au_4 monolayer has very obvious light absorption in the infrared, visible, and ultraviolet regions in the *z*-direction, while it only has strong absorption in the visible and ultraviolet regions in the *x*-direction. The intensity of light absorption in the visible region is particularly important because visible light contains almost half the energy of sunlight. In the visible-light region, the absorption coefficients in both the *x*- and *z*-directions reach 10^5 cm^{-1}, indicating a high absorption efficiency of solar energy. Moreover, it can be seen that the Au_4 monolayer has a stronger light absorption ability in the ultraviolet region.

https://doi.org/10.1021/acsomega.2c04391
ACS Omega 2022, 7, 32708−32716

Therefore, the Au_4 monolayer has a large absorption coefficient in the visible and ultraviolet regions and may be a very promising optoelectronic material in the future.

3.3. Geometric and Electronic Characters of the $Au_{16}(AuCl_2)_6$ Cluster. In a similar approach, we build an $Au_{16}(AuCl_2)_6$ cluster, which is composed of six [Cl−Au−Cl] ligands and an Au_{16} core. To highlight the Au core, we used a different color (blue) for the ligand Au atoms to distinguish them. The core of the $Au_{16}(AuCl_2)_6$ cluster contains five vertex-sharing Au_4 units, which are protected by six [Cl−Au−Cl] stable motifs. The optimized geometric configuration of $Au_{16}(AuCl_2)_6$ with a large E_{HL} of 2.47 eV is shown in Figure 5. The average Au−Au bond length is 2.72−2.75 Å. There are two types of Au−Cl bonds with bond lengths of 2.39 Å (connected with the Au_4 unit) and 2.32 Å (connected with the ligand Au atom). The chemical bonding pattern of $Au_{16}(AuCl_2)_6$ clusters is studied by the AdNDP method. As shown in Figure 5, there are five 4c-2e Au_4 σ bonds with ON = 1.86 |e|. In addition, two different Au−Cl σ bonds with ON = 1.97 |e| are also shown.

3.4. Geometric Structure, Stability, and Electronic Character of the Au_4 Crystal. The Au_{16} core of the $Au_{16}(AuCl_2)_6$ cluster is similar to an sp^3 hybrid C atom. Motivated by sp^3 hybrid C atoms in diamond, a super-tetrahedral structure can be designed by replacing C atoms with regular tetrahedral units, and some previous theoretical works have proved this.[90−92] Therefore, we use the diamond lattice as a template where all carbon atoms are substituted by Au_4 units, then connected all of the Au_4 units by sharing vertices to design a diamond-like Au_4 crystal. The fully optimized structure of the designed Au_4 crystal is shown in Figure 6a. One unit cell of the Au_4 crystal contains 16 Au atoms, the space group is $Fd\bar{3}m$ (number 227) and the lattice constants are $a = b = c = 7.76$ Å. All of the Au−Au bond lengths are 2.74 Å, slightly shorter than the average Au−Au bond length (2.77 Å) in the Au_4 monolayer. To gain insight into the chemical bonds in the Au_4 crystal, the SSAdNDP method was used. The SSAdNDP results indicate that there are five lone pairs of electrons on each Au atom (Figure S3), and another valence electron forms 4c-2e σ bonds in the Au_4 unit (Figure 6b). Thus, the Au_4 crystal can be viewed as a superatomic crystal stacked by Au_4 (2e) superatoms.

As shown in Table 2, compared with the gold in the classic fcc phase, the density of the Au_4 crystal is much smaller due to its larger pore size. The cohesive energy is calculated by $E_{coh} = (mE_{Au\text{-}atom} - E_{Au\text{-}bulk})/m$, where m, $E_{Au\text{-}atom}$, and $E_{Au\text{-}bulk}$ are the atom number, the total energies of a single Au atom, and one unit cell in the Au_4 crystal, respectively. The cohesive energy of the Au_4 crystal is 2.75 eV atom^{-1}, which is slightly smaller than that of the fcc-phase Au of 3.11 eV atom^{-1}. The Au_4 crystal has a higher strain strength and lower plasticity compared with the fcc-phase Au from the results of Young's modulus and Poisson's ratio value. Moreover, the Vickers hardness calculated with the same empirical formula[93] also illustrates this point. The computed phonon spectra of the Au_4 crystal exhibit all positive phonon frequencies (Figure 6c), confirming its dynamic stability. To test the thermal stability of the Au_4 crystal, we carry out AIMD simulations under an NVT ensemble with the temperature controlled at 300, 700, and 1000 K. Here, a supercell containing a 4 × 2 primitive cell (involving 128 Au atoms) was adopted as the initial configuration. The AIMD simulations lasted for 5 ps with a time step of 1 fs. As shown in Figure S4, after 5 ps simulations at 1000 K, the structure is still intact and the total energy remains almost unchanged, which suggests its high thermal stability. The Au_4 crystal can be used at extremely high temperatures.

Table 2. Density (ρ, g cm^{-3}), Cohesive Energy (E_{coh}, eV), Young's Modulus (E, GPa), Poisson's Ratio (ν), and Vickers Hardness (H, GPa) for the Au_4 Crystal[a]

structure	ρ	E_{coh}	E	ν	H
Au_4 bulk	11.18	2.75	173.00	0.20	13.65
fcc-Au	18.03	3.11	81.30	0.45	1.81

[a]For comparison, the experimental values of the fcc-Au structure are also given.

In comparison with the fcc-phase Au, the Au_4 crystal presents different structural properties and bonding patterns that may lead to unexpected physical properties. We calculated the band structure of the fcc-phase Au and the Au_4 crystal at the HSE06 level. As shown in Figure 7, both structures are metallic. The VB and conduction band (CB) of the fcc-phase Au are slightly overlapped, while the VB and CB of the Au_4 crystal phase are clearly separated, and there is a tendency to form a semiconductor. This may be due to the partial electronic localization in the Au_4 unit resulting from the special geometric structure of the Au_4 crystal. Similarly, we calculated the light absorption coefficients of the Au_4 crystal and fcc-phase Au by the HSE06 method, as shown in Figure S5. The area within the dotted line is in the visible-light range. We can clearly see that the Au_4 crystal and the fcc-phase Au have great light absorption in the visible and ultraviolet regions, and even their absorption coefficients in the ultraviolet region reach 10^6 cm^{-1}. The large absorption coefficient of the Au_4 crystal makes it a potential material for photovoltaic solar cells and optoelectronic devices.

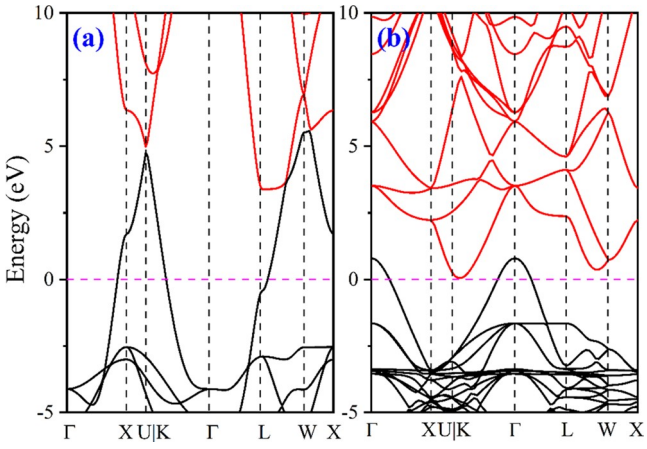

Figure 7. Electronic band structure of (a) fcc-phase Au and (b) Au_4 crystal at the HSE06 level. The Fermi level is set at zero and marked with pink dashed lines.

4. CONCLUSIONS

To summarize, we first adopt the Au_4 unit and [Cl−Au−Cl] as basic building blocks to construct $Au_7(AuCl_2)_3$, $Au_{12}(AuCl_2)_4$, $Au_{22}(AuCl_2)_6$, $Au_{30}(AuCl_2)_6$, and $Au_{16}(AuCl_2)_6$ clusters. DFT calculations show that each cluster is a real local minimum on the potential energy surface and has a large HOMO−LUMO

https://doi.org/10.1021/acsomega.2c04391
ACS Omega 2022, 7, 32708−32716

energy gap. In particular, the HOMO−LUMO energy gap of the $Au_7(AuCl_2)_3$ cluster is 2.47 eV. AdNDP and NICS analyses reveal that all of the structures follow the SAN model. Based on $Au_{30}(AuCl_2)_6$ and $Au_{16}(AuCl_2)_6$ clusters, we use the graphene and diamond as templates to design a graphene-like Au_4 monolayer and a diamond-like Au_4 crystal. The computational results demonstrate that both Au_4 monolayer and Au_4 crystal have a high dynamic, thermal, and mechanical stability. The Au_4 crystal can remain stable even at 1000 K. The cleavage energy of the Au_4 monolayer is similar to that of graphene, indicating that the exfoliation of its bulk form to achieve freestanding monolayers is very feasible. The calculated band structures of both the Au_4 monolayer and the Au_4 crystal at the HSE06 level show metallicity. The optical properties show that the Au_4 monolayer has a large light absorption coefficient. The SSAdNDP analyses indicate that these two structures are composed of Au_4 (2e) units, thus they can be viewed as superatomic crystals. All these findings provide new insights for the study of thiolate-protected gold nanoclusters. In addition, we predicted two new types of superatom crystal gold, enriching the structure types of gold.

■ ASSOCIATED CONTENT

Supporting Information

The Supporting Information is available free of charge at https://pubs.acs.org/doi/10.1021/acsomega.2c04391.

SSAdNDP chemical bonding patterns of the Au_4 monolayer and the Au_4 crystal; AIMD simulation of the Au_4 monolayer and the Au_4 crystal; optical absorption spectra of the Au_4 crystal and the fcc-phase Au; and *xyz* coordinates of all structures after optimization (PDF)

■ AUTHOR INFORMATION

Corresponding Authors

Dan Li − *Department of Chemistry, Key Laboratory of Functional Inorganic Materials of Anhui Province, Anhui University, Hefei, Anhui 230601, P. R. China*; Email: ahulidan@aliyun.com

Longjiu Cheng − *Department of Chemistry, Key Laboratory of Functional Inorganic Materials of Anhui Province, Anhui University, Hefei, Anhui 230601, P. R. China; Key Laboratory of Structure and Functional Regulation of Hybrid Materials, Anhui University, Ministry of Education, Hefei 230601, P. R. China;* orcid.org/0000-0001-7086-6190; Email: clj@ustc.edu

Authors

Chen Yan − *Department of Chemistry, Key Laboratory of Functional Inorganic Materials of Anhui Province, Anhui University, Hefei, Anhui 230601, P. R. China*

Jiuqi Yi − *Department of Chemistry, Key Laboratory of Functional Inorganic Materials of Anhui Province, Anhui University, Hefei, Anhui 230601, P. R. China*

Peng Wang − *Department of Chemistry, Key Laboratory of Functional Inorganic Materials of Anhui Province, Anhui University, Hefei, Anhui 230601, P. R. China*

Complete contact information is available at: https://pubs.acs.org/10.1021/acsomega.2c04391

Notes

The authors declare no competing financial interest.

■ ACKNOWLEDGMENTS

This work is financed by the National Natural Science Foundation of China (21873001) and the Foundation of Distinguished Young Scientists of Anhui Province. The calculations are carried out at the High-Performance Computing Center of Anhui University.

■ REFERENCES

(1) Jin, R.; Zeng, C.; Zhou, M.; Chen, Y. Atomically Precise Colloidal Metal Nanoclusters and Nanoparticles: Fundamentals and Opportunities. *Chem. Rev.* **2016**, *116*, 10346−10413.

(2) Häkkinen, H. The Gold−Sulfur Interface at the Nanoscale. *Nat. Chem.* **2012**, *4*, 443−455.

(3) Jin, R.; Li, G.; Sharma, S.; Li, Y.; Du, X. Toward Active-Site Tailoring in Heterogeneous Catalysis by Atomically Precise Metal Nanoclusters with Crystallographic Structures. *Chem. Rev.* **2021**, *121*, 567−648.

(4) Kang, X.; Zhu, M. Cocrystallization of Atomically Precise Nanoclusters. *ACS Mater. Lett.* **2020**, *2*, 1303−1314.

(5) Yang, L.; Wang, P.; Yang, Z.; Pei, Y. Effect of Thiolate-Ligand Passivation on the Electronic Structure and Optical Absorption Properties of Ultrathin One and Two-Dimensional Gold Nanocrystals. *Nanoscale* **2020**, *12*, 5554−5566.

(6) Rosi, N. L.; Giljohann, D. A.; Thaxton, C. S.; Lytton-Jean, A. K. R.; Han, M. S.; Mirkin, C. A. Oligonucleotide-Modified Gold Nanoparticles for Intracellular Gene Regulation. *Science* **2006**, *312*, 1027−1030.

(7) Knoppe, S.; Dolamic, I.; Dass, A.; Burgi, T. Separation of Enantiomers and Cd Spectra of Au40(Sch2ch2ph)24: Spectroscopic Evidence for Intrinsic Chirality. *Angew. Chem., Int. Ed.* **2012**, *51*, 7589−7591.

(8) Jadzinsky, P. D.; Calero, G.; Ackerson, C. J.; Bushnell, D. A.; Kornberg, R. D. Structure of a Thiol Monolayer-Protected Gold Nanoparticle at 1.1 Å Resolution. *Science* **2007**, *318*, 430−433.

(9) Zhu, M.; Aikens, C. M.; Hollander, F. J.; Schatz, G. C.; Jin, R. Correlating the Crystal Structure of a Thiol-Protected Au25 Cluster and Optical Properties. *J. Am. Chem. Soc.* **2008**, *130*, 5883−5885.

(10) Heaven, M. W.; Dass, A.; White, P. S.; Holt, K. M.; Murray, R. W. Crystal Structure of the Gold Nanoparticle [N(C8h17)4][Au25-(Sch2ch2ph)18]. *J. Am. Chem. Soc.* **2008**, *130*, 3754−3755.

(11) Xie, J.; Zheng, Y.; Ying, J. Y. Protein-Directed Synthesis of Highly Fluorescent Gold Nanoclusters. *J. Am. Chem. Soc.* **2009**, *131*, 888−889.

(12) Jin, R. Quantum Sized, Thiolate-Protected Gold Nanoclusters. *Nanoscale* **2010**, *2*, 343−362.

(13) Shang, L.; Dong, S.; Nienhaus, G. U. Ultra-Small Fluorescent Metal Nanoclusters: Synthesis and Biological Applications. *Nano Today* **2011**, *6*, 401−418.

(14) Du, Y.; Sheng, H.; Astruc, D.; Zhu, M. Atomically Precise Noble Metal Nanoclusters as Efficient Catalysts: A Bridge between Structure and Properties. *Chem. Rev.* **2020**, *120*, 526−622.

(15) Fan, Y.; Liu, S.; Yi, Y.; Rong, H.; Zhang, J. Catalytic Nanomaterials toward Atomic Levels for Biomedical Applications: From Metal Clusters to Single-Atom Catalysts. *ACS Nano* **2021**, *15*, 2005−2037.

(16) Kang, X.; Li, Y.; Zhu, M.; Jin, R. Atomically Precise Alloy Nanoclusters: Syntheses, Structures, and Properties. *Chem. Soc. Rev.* **2020**, *49*, 6443−6514.

(17) Pei, Y.; Lin, S.; Su, J.; Liu, C. Structure Prediction of Au44(Sr)28: A Chiral Superatom Cluster. *J. Am. Chem. Soc.* **2013**, *135*, 19060−19063.

(18) Natarajan, G.; Mathew, A.; Negishi, Y.; Whetten, R. L.; Pradeep, T. A Unified Framework for Understanding the Structure and Modifications of Atomically Precise Monolayer Protected Gold Clusters. *J. Phys. Chem. C* **2015**, *119*, 27768−27785.

(19) Taylor, M. G.; Mpourmpakis, G. Thermodynamic Stability of Ligand-Protected Metal Nanoclusters. *Nat. Commun.* **2017**, *8*, No. 15988.

(20) Muñoz-Castro, A. Au70s20(Pph3)(12) as Superatomic Analog to 18-Electron Transition-Metal Complexes. *Z. Anorg. Allg. Chem.* **2021**, *647*, 1819−1823.
(21) Muñoz-Castro, A. Sp(3)-Hybridization in Superatomic Clusters. Analogues to Simple Molecules Involving the Au-6 Core. *Chem. Sci.* **2014**, *5*, 4749−4754.
(22) Han, W.; Liu, P.; Zheng, M.; Zeng, X. C.; Xu, W. W. Ring Model for Understanding How Interfacial Interaction Dictates the Structures of Protection Motifs and Gold Cores in Thiolate-Protected Gold Nanoclusters. *J. Phys. Chem. Lett.* **2021**, *12*, 3006−3013.
(23) Pei, Y.; Zeng, X. C. Investigating the Structural Evolution of Thiolate Protected Gold Clusters from First-Principles. *Nanoscale* **2012**, *4*, 4054−4072.
(24) Häkkinen, H.; Walter, M.; Grönbeck, H. Divide and Protect: Capping Gold Nanoclusters with Molecular Gold−Thiolate Rings. *J. Phys. Chem. B* **2006**, *110*, 9927−9931.
(25) Lopez-Acevedo, O.; Akola, J.; Whetten, R. L.; Gronbeck, H.; Hakkinen, H. Structure and Bonding in the Ubiquitous Icosahedral Metallic Gold Cluster Au144(Sr)(60). *J. Phys. Chem. C* **2009**, *113*, 5035−5038.
(26) Knoppe, S.; Wong, O. A.; Malola, S.; Hakkinen, H.; Burgi, T.; Verbiest, T.; Ackerson, C. J. Chiral Phase Transfer and Enantioenrichment of Thiolate-Protected Au102 Clusters. *J. Am. Chem. Soc.* **2014**, *136*, 4129−4132.
(27) Xu, W. W.; Gao, Y.; Zeng, X. C. Unraveling Structures of Protection Ligands on Gold Nanoparticle Au68(Sh)(32). *Adv. Sci.* **2015**, *1*, No. e1400211.
(28) Xu, W. W.; Li, Y. D.; Gao, Y.; Zeng, X. C. Medium-Sized Au40(Sr)(24) and Au52(Sr)(32) Nanoclusters with Distinct Gold-Kernel Structures and Spectroscopic Features. *Nanoscale* **2016**, *8*, 1299−1304.
(29) Xu, W. W.; Zeng, X. C.; Gao, Y. The Structural Isomerism in Gold Nanoclusters. *Nanoscale* **2018**, *10*, 9476−9483.
(30) Ma, Z. Y.; Wang, P.; Xiong, L.; Pei, Y. Thiolate-Protected Gold Nanoclusters: Structural Prediction and the Understandings of Electronic Stability from First Principles Simulations. *WIREs Comput. Mol. Sci.* **2017**, *7*, No. e1315.
(31) Pei, Y.; Gao, Y.; Zeng, X. C. Structural Prediction of Thiolate-Protected Au38: A Face-Fused Bi-Icosahedral Au Core. *J. Am. Chem. Soc.* **2008**, *130*, 7830−7832.
(32) Schaaff, T. G.; Shafigullin, M. N.; Khoury, J. T.; Vezmar, I.; Whetten, R. L.; Cullen, W. G.; First, P. N.; Gutiérrez-Wing, C.; Ascensio, J.; Jose-Yacamán, M. J. Isolation of Smaller Nanocrystal Au Molecules: Robust Quantum Effects in Optical Spectra. *J. Phys. Chem. B* **1997**, *101*, 7885−7891.
(33) Qian, H.; Eckenhoff, W. T.; Zhu, Y.; Pintauer, T.; Jin, R. Total Structure Determination of Thiolate-Protected Au38 Nanoparticles. *J. Am. Chem. Soc.* **2010**, *132*, 8280−8281.
(34) Walter, M.; Akola, J.; Lopez-Acevedo, O.; Jadzinsky, P. D.; Calero, G.; Ackerson, C. J.; Whetten, R. L.; Grönbeck, H.; Häkkinen, H. A Unified View of Ligand-Protected Gold Clusters as Superatom Complexes. *Proc. Natl. Acad. Sci. U.S.A.* **2008**, *105*, 9157−9162.
(35) Jiang, D.-e.; Overbury, S. H.; Dai, S. Structure of Au15(Sr)13 and Its Implication for the Origin of the Nucleus in Thiolated Gold Nanoclusters. *J. Am. Chem. Soc.* **2013**, *135*, 8786−8789.
(36) Liao, L.; Zhuang, S.; Yao, C.; et al. Structure of Chiral Au44(2,4-Dmbt)26 Nanocluster with an 18-Electron Shell Closure. *J. Am. Chem. Soc.* **2016**, *138*, 10425−10428.
(37) Cheng, L.; Yang, J. Communication: New Insight into Electronic Shells of Metal Clusters: Analogues of Simple Molecules. *J. Chem. Phys.* **2013**, *138*, No. 141101.
(38) Xu, C.; Zhou, Y. C.; Yi, J. Q.; Li, D.; Shi, L. L.; Cheng, L. J. Tri- and Tetra-Superatomic Molecules in Ligand-Protected Face-Fused Icosahedral (M@Au-12)(N) (M = Au, Pt, Ir, and Os, and N=3 and 4) Clusters. *J. Phys. Chem. Lett.* **2022**, *13*, 1931−1939.
(39) Zhou, Y. C.; Yu, X. L.; Cheng, L. J. Multiple D-D Bonds between Early Transition Metals in Tm2lin(Tm = Sc, Ti) Superatomic Molecule Clusters. *Nanoscale* **2020**, *12*, 20506−20512.
(40) Cheng, L.; Ren, C.; Zhang, X.; Yang, J. New Insight into the Electronic Shell of Au-38(Sr)(24): A Superatomic Molecule. *Nanoscale* **2013**, *5*, 1475−1478.
(41) Cheng, L.; Yuan, Y.; Zhang, X.; Yang, J. Superatom Networks in Thiolate-Protected Gold Nanoparticles. *Angew. Chem., Int. Ed.* **2013**, *52*, 9035−9039.
(42) Tian, Z. M.; Xu, Y. Y.; Cheng, L. J. New Perspectives on the Electronic and Geometric Structure of Au70s20(Pph3)(12) Cluster: Superatomic-Network Core Protected by Novel Au12(Mu(3)-S)(10) Staple Motifs. *Nanomaterials* **2019**, *9*, No. 1132.
(43) Reilly, S. M.; Krick, T.; Dass, A. Surfactant-Free Synthesis of Ultrasmall Gold Nanoclusters. *J. Phys. Chem. C* **2010**, *114*, 741−745.
(44) Zhu, M.; Qian, H.; Jin, R. Thiolate-Protected Au20 Clusters with a Large Energy Gap of 2.1 Ev. *J. Am. Chem. Soc.* **2009**, *131*, 7220−7221.
(45) Pei, Y.; Tang, J.; Tang, X. Q.; Huang, Y. Q.; Zeng, X. C. New Structure Model of Au-22(Sr)(18): Bitetrahederon Golden Kernel Enclosed by Au-6(Sr)(6) Au(I) Complex. *J. Phys. Chem. Lett.* **2015**, *6*, 1390−1395.
(46) Zhu, M.; Qian, H.; Jin, R. Thiolate-Protected Au24(Sc2h4ph)-20 Nanoclusters: Superatoms or Not? *J. Phys. Chem. Lett.* **2010**, *1*, 1003−1007.
(47) Pei, Y.; Wang, P.; Ma, Z.; Xiong, L. Growth-Rule-Guided Structural Exploration of Thiolate-Protected Gold Nanoclusters. *Acc. Chem. Res.* **2019**, *52*, 23−33.
(48) Xiong, L.; Yang, S.; Sun, X.; Chai, J.; Rao, B.; Yi, L.; Zhu, M.; Pei, Y. Structure and Electronic Structure Evolution of Thiolate-Protected Gold Nanoclusters Containing Quasi Face-Centered-Cubic Kernels. *J. Phys. Chem. C* **2018**, *122*, 14898−14907.
(49) Liu, X.; Xu, W. W.; Huang, X.; et al. De Novo Design of Au36(Sr)(24) Nanoclusters. *Nat. Commun.* **2020**, *11*, No. 3349.
(50) Zeng, C. J.; Chen, Y. X.; Liu, C.; Nobusada, K.; Rosi, N. L.; Jin, R. C. Gold Tetrahedra Coil Up: Kekule-Like and Double Helical Superstructures. *Adv. Sci.* **2015**, *1*, No. e1500425.
(51) Xu, W. W.; Li, Y. D.; Gao, Y.; Zeng, X. C. Unraveling a Generic Growth Pattern in Structure Evolution of Thiolate-Protected Gold Nanoclusters. *Nanoscale* **2016**, *8*, 7396−7401.
(52) Ma, Z. Y.; Wang, P.; Zhou, G.; Tang, J.; Li, H. F.; Pei, Y. Correlating the Structure and Optical Absorption Properties of Au76(Sr)44 Cluster. *J. Phys. Chem. C* **2016**, *120*, 13739−13748.
(53) Zeng, C.; Chen, Y.; Iida, K.; Nobusada, K.; Kirschbaum, K.; Lambright, K. J.; Jin, R. Gold Quantum Boxes: On the Periodicities and the Quantum Confinement in the Au28, Au36, Au44, and Au52 Magic Series. *J. Am. Chem. Soc.* **2016**, *138*, 3950−3953.
(54) Yang, L.-M.; Ganz, A. B.; Dornfeld, M.; Ganz, E. Computational Study of Quasi-2d Liquid State in Free Standing Platinum, Silver, Gold, and Copper Monolayers. *Condens. Matter* **2016**, *1*, No. 1.
(55) Yang, L. M.; Frauenheim, T.; Ganz, E. Properties of the Free-Standing Two-Dimensional Copper Monolayer. *J. Nanomater.* **2016**, *2016*, No. 8429510.
(56) Liu, P.; Han, W.; Zheng, M.; Xu, W. W. Two-Dimensional Growth Mode of Thiolate-Protected Gold Nanoclusters Au28+4n-(Sr)20+2n (N = 0−8): Compared with Their One-Dimensional Growth Mode. *Nanoscale* **2020**, *12*, 20677−20683.
(57) Liu, Q.; Zhang, C.; Xu, C.; Hu, S.; Cheng, L. Prediction of the Au4s Crystal Via a Superatom Network Model: From Clusters to Solids. *Phys. Chem. Chem. Phys.* **2020**, *22*, 3921−3926.
(58) Yang, L.-M.; Dornfeld, M.; Frauenheim, T.; Ganz, E. Glitter in a 2d Monolayer. *Phys. Chem. Chem. Phys.* **2015**, *17*, 26036−26042.
(59) Yang, L. M.; Frauenheim, T.; Ganz, E. The New Dimension of Silver. *Phys. Chem. Chem. Phys.* **2015**, *17*, 19695−19699.
(60) Perdew, J. P.; Burke, K.; Ernzerhof, M. Generalized Gradient Approximation Made Simple. *Phys. Rev. Lett.* **1996**, *77*, 3865−3868.
(61) Weigend, F.; Ahlrichs, R. Balanced Basis Sets of Split Valence, Triple Zeta Valence and Quadruple Zeta Valence Quality for H to Rn: Design and Assessment of Accuracy. *Phys. Chem. Chem. Phys.* **2005**, *7*, 3297−3305.
(62) Frisch, M.; Trucks, G.; Schlegel, H.; Scuseria, G.; Robb, M.; Cheeseman, J.; Scalmani, G.; Barone, V.; Mennucci, B.; Petersson, G.

https://doi.org/10.1021/acsomega.2c04391
ACS Omega 2022, 7, 32708−32716

J. W. *Gaussian 09*; Gaussian, Inc.: Wallingford, CT, 2009; Vol. *32*, pp 5648−5652.
(63) Nair, L. V.; Hossain, S.; Takagi, S.; Imai, Y.; Hu, G.; Wakayama, S.; Kumar, B.; Kurashige, W.; Jiang, D.-e.; Negishi, Y. Hetero-Biicosahedral [Au24pd(Pph3)10(Sc2h4ph)5cl2]+ Nanocluster: Selective Synthesis and Optical and Electrochemical Properties. *Nanoscale* **2018**, *10*, 18969−18979.
(64) Kresse, G.; Furthmüller, J. Efficient Iterative Schemes for Ab Initio Total-Energy Calculations Using a Plane-Wave Basis Set. *Phys. Rev. B: Condens. Matter Mater. Phys.* **1996**, *54*, 11169−11186.
(65) Blöchl, P. E. Projector Augmented-Wave Method. *Phys. Rev. B: Condens. Matter Mater. Phys.* **1994**, *50*, 17953−17979.
(66) Paier, J.; Hirschl, R.; Marsman, M.; Kresse, G. The Perdew−Burke−Ernzerhof Exchange-Correlation Functional Applied to the G2-1 Test Set Using a Plane-Wave Basis Set. *J. Chem. Phys.* **2005**, *122*, No. 234102.
(67) Grimme, S.; Antony, J.; Ehrlich, S.; Krieg, H. A Consistent and Accurate Ab Initio Parametrization of Density Functional Dispersion Correction (Dft-D) for the 94 Elements H-Pu. *J. Chem. Phys.* **2010**, *132*, No. 154104.
(68) Togo, A.; Tanaka, I. First Principles Phonon Calculations in Materials Science. *Scr. Mater.* **2015**, *108*, 1−5.
(69) Martyna, G. J.; Klein, M. L.; Tuckerman, M. Nosé−Hoover Chains: The Canonical Ensemble Via Continuous Dynamics. *J. Chem. Phys.* **1992**, *97*, 2635−2643.
(70) Heyd, J.; Scuseria, G. E.; Ernzerhof, M. Hybrid Functionals Based on a Screened Coulomb Potential. *J. Chem. Phys.* **2003**, *118*, 8207−8215.
(71) Zubarev, D. Y.; Boldyrev, A. I. Revealing Intuitively Assessable Chemical Bonding Patterns in Organic Aromatic Molecules Via Adaptive Natural Density Partitioning. *J. Org. Chem.* **2008**, *73*, 9251−9258.
(72) Zubarev, D. Y.; Boldyrev, A. I. "Developing Paradigms of Chemical Bonding: Adaptive Natural Density Partitioning. *Phys. Chem. Chem. Phys.* **2008**, *10*, 5207−5217.
(73) Galeev, T. R.; Dunnington, B. D.; Schmidt, J. R.; Boldyrev, A. I. Solid State Adaptive Natural Density Partitioning: A Tool for Deciphering Multi-Center Bonding in Periodic Systems. *Phys. Chem. Chem. Phys.* **2013**, *15*, 5022−5029.
(74) Steglenko, D. V.; Tkachenko, N. V.; Boldyrev, A. I.; Minyaev, R. M.; Minkin, V. I. Stability, Electronic, and Optical Properties of Two-Dimensional Phosphoborane. *J. Comput. Chem.* **2020**, *41*, 1456−1463.
(75) Fedik, N.; Boldyrev, A. I.; Muñoz-Castro, A. Aromatic Character of [Au13]5+ and [Mau12]4+/6+ (M = Pd, Pt) Cores in Ligand Protected Gold Nanoclusters − Interplay between Spherical and Planar ∑-Aromatics. *Phys. Chem. Chem. Phys.* **2019**, *21*, 25215−25219.
(76) Yi, J.; Gong, B.; Xu, C.; Zhang, W.; Cheng, L. Prediction of an Al4c4 Superatom Organic Framework (Sof) Material Based on the Superatom Network Model. *Phys. Chem. Chem. Phys.* **2021**, *23*, 24294−24300.
(77) Zeng, C.; Liu, C.; Chen, Y.; Rosi, N. L.; Jin, R. Gold−Thiolate Ring as a Protecting Motif in the Au20(Sr)16 Nanocluster and Implications. *J. Am. Chem. Soc.* **2014**, *136*, 11922−11925.
(78) Sun, X.; Wang, P.; Xiong, L.; Pei, Y. Theoretical Prediction of a New Stable Structure of Au28(Sr)20 Cluster. *Chem. Phys. Lett.* **2018**, *704*, 68−75.
(79) Stanger, A. Nucleus-Independent Chemical Shifts (Nics): Distance Dependence and Revised Criteria for Aromaticity and Antiaromaticity. *J. Org. Chem.* **2006**, *71*, 883−893.
(80) Schleyer, P. v. R.; Manoharan, M.; Wang, Z.-X.; Kiran, B.; Jiao, H.; Puchta, R.; van Eikema Hommes, N. J. R. Dissected Nucleus-Independent Chemical Shift Analysis of Π-Aromaticity and Antiaromaticity. *Org. Lett.* **2001**, *3*, 2465−2468.
(81) Song, B. Y.; Zhou, Y.; Yang, H. M.; Liao, J. H.; Yang, L. M.; Yang, X. B.; Ganz, E. Two-Dimensional Anti-Van't Hoff/Le Bel Array Alb6 with High Stability, Unique Motif, Triple Dirac Cones, and Superconductivity. *J. Am. Chem. Soc.* **2019**, *141*, 3630−3640.
(82) Yang, L. M.; Bacic, V.; Popov, I. A.; Boldyrev, A. I.; Heine, T.; Frauenheim, T.; Ganz, E. Two-Dimensional Cu2si Monolayer with Planar Hexacoordinate Copper and Silicon Bonding. *J. Am. Chem. Soc.* **2015**, *137*, 2757−2762.
(83) Yang, L. M.; Popov, I. A.; Boldyrev, A. I.; Heine, T.; Frauenheim, T.; Ganz, E. Post-Anti-Van't Hoff-Le Bel Motif in Atomically Thin Germanium-Copper Alloy Film. *Phys. Chem. Chem. Phys.* **2015**, *17*, 17545−17551.
(84) Qin, G.; Yan, Q.-B.; Qin, Z.; Yue, S.-Y.; Hu, M.; Su, G. Anisotropic Intrinsic Lattice Thermal Conductivity of Phosphorene from First Principles. *Phys. Chem. Chem. Phys.* **2015**, *17*, 4854−4858.
(85) Lee, C.; Yan, H.; Brus, L. E.; Heinz, T. F.; Hone, J.; Ryu, S. Anomalous Lattice Vibrations of Single- and Few-Layer Mos2. *ACS Nano* **2010**, *4*, 2695−2700.
(86) Coleman, J. N.; Lotya, M.; O'Neill, A.; et al. Two-Dimensional Nanosheets Produced by Liquid Exfoliation of Layered Materials. *Science* **2011**, *331*, 568−571.
(87) Jing, Y.; Liu, J.; Zhou, Z. P.; Zhang, J.; Li, Y. F. Metallic Nb2s2c Monolayer: A Promising Two-Dimensional Anode Material for Metal-Ion Batteries. *J. Phys. Chem. C* **2019**, *123*, 26803−26811.
(88) Ziambaras, E.; Kleis, J.; Schroder, E.; Hyldgaard, P. Potassium Intercalation in Graphite: A Van Der Waals Density-Functional Study. *Phys. Rev. B* **2007**, *76*, No. 155425.
(89) Zacharia, R.; Ulbricht, H.; Hertel, T. Interlayer Cohesive Energy of Graphite from Thermal Desorption of Polyaromatic Hydrocarbons. *Phys. Rev. B* **2004**, *69*, No. 155406.
(90) Burdett, J. K.; Lee, S. Moments Method and Elemental Structures. *J. Am. Chem. Soc.* **1985**, *107*, 3063−3082.
(91) Getmanskii, I. V.; Minyaev, R. M.; Steglenko, D. V.; Koval, V. V.; Zaitsev, S. A.; Minkin, V. I. From Two- to Three-Dimensional Structures of a Supertetrahedral Boran Using Density Functional Calculations. *Angew. Chem., Int. Ed.* **2017**, *56*, 10118−10122.
(92) Getmanskii, I. V.; Koval, V. V.; Minyaev, R. M.; Boldyrev, A. I.; Minkin, V. I. Supertetrahedral Aluminum − a New Allotropic Ultralight Crystalline Form of Aluminum. *J. Phys. Chem. C* **2017**, *121*, 22187−22190.
(93) Xu, B.; Tian, Y. Superhard Materials: Recent Research Progress and Prospects. *Sci. China Mater.* **2015**, *58*, 132−142.

https://doi.org/10.1021/acsomega.2c04391
ACS Omega 2022, 7, 32708−32716